THE JOURNAL OF PHYSICAL CHEMISTRY B

Article

pubs.acs.org/JPCB

Photoabsorption of Acridine Yellow and Proflavin Bound to Human Serum Albumin Studied by Means of Quantum Mechanics/Molecular Dynamics

Kęstutis Aidas,*[,†] Jógvan Magnus H. Olsen,[‡] Jacob Kongsted,[‡] and Hans Ågren[§]

[†]Department of General Physics and Spectroscopy, Faculty of Physics, Vilnius University, Saulėtekio al. 9, LT-10222 Vilnius, Lithuania

[‡]Department of Physics, Chemistry and Pharmacy, University of Southern Denmark, Campusvej 55, DK-5230 Odense M, Denmark

[§]Department of Theoretical Chemistry and Biology, School of Biotechnology, Royal Institute of Technology, SE-10691 Stockholm, Sweden

ABSTRACT: Attempting to unravel mechanisms in optical probing of proteins, we have performed pilot calculations of two cationic chromophores—acridine yellow and proflavin—located at different binding sites within human serum albumin, including the two primary drug binding sites as well as a heme binding site. The computational scheme adopted involves classical molecular dynamics simulations of the ligands bound to the protein and subsequent linear response polarizable embedding density functional theory calculations of the excitation energies. A polarizable embedding potential consisting of point charges fitted to reproduce the electrostatic potential and isotropic atomic polarizabilities computed individually for every residue of the protein was used in the linear response calculations. Comparing the calculated aqueous solution-to-protein shifts of maximum absorption energies to available experimental data, we concluded that the cationic proflavin chromophore is likely not to bind albumin at its drug binding site 1 nor at its heme binding site. Although agreement with experimental data could only be obtained in qualitative terms, our results clearly indicate that the difference in optical response of the two probes is due to deprotonation, and not, as earlier suggested, to different binding sites. The ramifications of this finding for design of molecular probes targeting albumin or other proteins is briefly discussed.

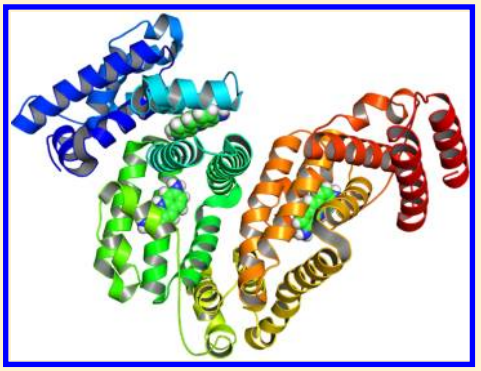

I. INTRODUCTION

Many important biological functions of human serum albumin (HSA), the most abundant protein in human circulation, are rooted in its ability to bind a variety of species ranging from atomic ions and small molecules to macromolecular compounds such as dendrimers, fullerene derivatives, and proteins.[1−9] Transport and storage of fatty acids, hormones, metals, and drugs, enhancement in solubility of otherwise water-insoluble molecules, and neutralization of toxins are among well-documented functions of HSA.[1−3,6] In addition, HSA is responsible for around 80% of the serum's oncotic pressure, and it exhibits antioxidant as well as enzymatic properties and influences pharmacokinetics and drug metabolism.[1−3,10−12] Albumin also serves as a natural biomarker of diseases such as cancer, arthritis, and ischemia.[3] Gene manipulation techniques have opened the door for an effective synthesis of recombinant HSA and its mutants having desired therapeutic properties.[3,13−16] Development of novel drugs where recombinant albumin dimers act as delivery vehicles has in some instances entered the stage of clinical trials.[17,18] Furthermore, the possibilities to use genetically engineered recombinant HSA as an artificial oxygen carrier have been explored.[19]

HSA is a monomeric helical protein consisting of 585 natural amino acids, and 17 disulfide bridges assist in maintaining its familiar heart-like shape.[1,20] Albumin's single polypeptide chain is composed of three structurally similar domains I, II, and III, linked by interdomain helices (see Figure 1). Each domain is further divided into A and B subdomains containing 6 and 4 α-helices, respectively, all connected by random coils. A multitude of ligand binding sites are scattered over the entire protein. There are nine distinct fatty acid binding sites,[3,6,9] four thyroxine binding sites,[3] several metal binding sites including albumin's N-terminus, and a site centered around residue Cys34.[1,3] The Cys34 residue is also a known reactive center for many genotoxic carcinogens leading to the formation of carcinogen−HSA adducts.[21] Heme binds albumin at the site in subdomain IB (heme-BS) where it interferes with the π-stacked configuration of residues Tyr138 and Tyr161.[22,23] The two primary drug binding sites 1 and 2 (BS1 and BS2), first characterized by Sudlow et al.,[24] are located in subdomains IIA and IIIA, respectively;[20] see Figure 1. While the entrance to the

Received: December 3, 2012
Revised: January 22, 2013
Published: January 28, 2013

dx.doi.org/10.1021/jp311863x | J. Phys. Chem. B 2013, 117, 2069−2080

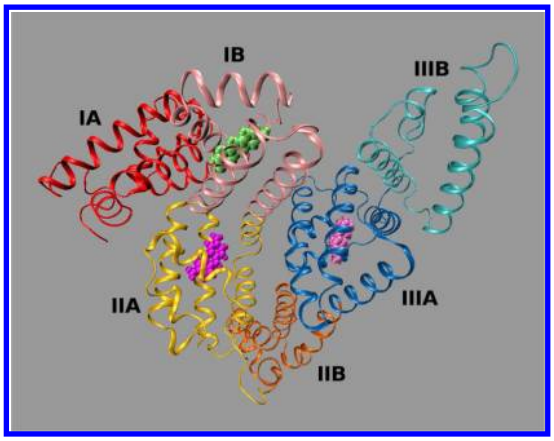

Figure 1. Domain structure of HSA (based on pdb id 1N5U). Colored ligands indicate considered binding sites of HSA—BS1 (magenta), BS2 (mauve), and heme-BS (lime).

large and flexible multichamber BS1 is surrounded by polar and positively charged residues like Arg218, Arg222, Arg257, Lys195, and Lys199, the interior is essentially hydrophobic. BS2 is smaller and more rigid as compared to BS1, and the opening to the binding pocket is rather exposed to solvent. Residues Tyr410 and Arg411 are usually considered to be important in relation to ligand binding at BS2. We refer to refs 2, 6, and 25 for a detailed account of the structural features of BS1 and BS2.

Typically, negatively charged or neutral acidic and/or aromatic heterocyclic drugs bind at BS1 or BS2 selectively.[2,4,10,20,25,26] Although cationic drugs usually bind α_1-acid glycoprotein in serum,[27] some have also been reported to bind HSA, yet very little is known regarding their preferred binding sites.[1,2,4,28] By combining a variety of spectroscopic techniques, Chakraborty et al.[29] have recently succeeded to track down the binding of two acridine-based cationic dye molecules, acridine yellow (AY) and proflavin (PF), to defatted HSA; see Figure 2.

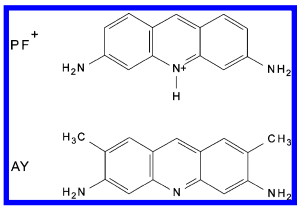

Figure 2. Structures of cationic proflavin, PF^+, and acridine yellow, AY.

A very curious behavior of the lowest electronic absorption band of the two ligands was recorded: compared to their absorption in dilute aqueous solution, a marked blue shift of 0.33 eV was seen upon AY binding albumin, while the absorption band of PF showed just a minor red shift of −0.03 eV. An attempt to interpret this finding lead the authors to propose that AY binds within a hydrophobic cavity and PF forms hydrogen bonding with albumin.[29] Both dyes exist in the cationic protonated forms (AY^+ and PF^+) in aqueous solution at pH around 7.[30,31] However, AY binds to HSA in its neutral deprotonated form, whereas PF^+ retains its cationic state while interacting with the protein;[29] see Figure 2. Deprotonation of PF^+ in aqueous solution at pH above 9.5 is accompanied by a blue shift of the lowest absorption band by 0.36 eV,[30,32] and it is plausible to assume a similar shift for AY due to the close similarity between the two acridine derivatives. In light of this, the character of the microenvironment felt by AY bound to HSA can hardly be judged.

We have initiated this study to rationalize the peculiarities of the electronic absorption of AY and PF^+ bound to albumin observed in the work of Chakraborty et al. Our approach is based on an integrated molecular modeling scheme comprising molecular dynamics (MD) simulations and polarizable embedding density functional theory (PE-DFT) methods. Classical MD simulations have already served the purpose to expose the structural and dynamical aspects of ligand binding to HSA.[33−36] The strength of our approach lies particularly in the PE-DFT model which provides an effective description of electrostatic and mutual many-body polarization interactions between the quantum and classical regions of the partitioned system, yielding vertical excitation energies through the linear response method.[37,38] This physically sound yet cost-effective polarizable embedding scheme allows to represent the entire albumin protein by a polarizable embedding potential. The parameters of the latter are derived from electronic structure calculations on individual residues according to the technique of molecular fractionation with conjugate caps.[39] The linear response PE-DFT model has already demonstrated its potential in recent theoretical photoabsorption studies on photoactive yellow protein, green fluorescent protein, DsRed, and β-lactoglobulin.[40−43] In this work, our spotlight is first of all on both ligands AY and PF bound at the two primary drug binding sites BS1 and BS2, but also at the heme-BS (see Figure 1), the choice based on the outcome from our molecular docking studies (vide infra). By comparing the predicted and measured spectroscopic observables, we hope to be able to confirm or deny the possible binding of AY and PF at these three high-affinity binding sites of HSA, to contribute to a better understanding of the cationic ligand binding to HSA, and to unravel more precisely what is the cause of the salient optical shifts of these probes that follow upon the binding.

II. METHODS

A. MD Simulations. The Amber11 suite of programs[44] was employed to conduct MD simulations in this work. The condensed-phase C_2 geometries of AY and AY^+ as well as the C_{2v} geometry of PF^+ were optimized at the HF/6-31G* level[45,46] in vacuum using the Gaussian09 program.[47] Dye molecules were represented by the general Amber force field[48,49] (GAFF). Atomic point charges for the chromophores were derived by means of the restrained electrostatic potential (RESP) procedure[50] implemented in the Antechamber module[51] of Amber11. In the simulations of AY^+ and PF^+ aqueous solutions, the RESP-derived charges for the solutes are based on the HF/6-31G* electrostatic potentials computed using Gaussian09. The microenvironment provided by the considered binding sites of albumin is seemingly less polar as compared to the pure aqueous medium. We have thereby relied on the B3LYP/cc-pVTZ method[52−54] in combination with the polarizable continuum model[55,56] (PCM) with the static dielectric constant of 4.0 to calculate electrostatic potentials for RESP-fitting of the point charges for the dye molecules to be used in their simulations within the protein. Default settings of PCM as implemented in Gaussian09 were used in these calculations apart from the modified dielectric constant. The TIP3P force field[57] was adopted for water molecules in the MD simulations. A single Cl^- anion was added to neutralize the systems of aqueous AY^+ and PF^+.

dx.doi.org/10.1021/jp311863x | J. Phys. Chem. B 2013, 117, 2069−2080

An X-ray structure of HSA[22] (pdb code 1N5U) obtained at a resolution of 1.9 Å was used as the starting point of the MD simulations. The five myristic acids, heme, and all water molecules present in the crystallographic structure were removed. To determine protonation states of acidic and basic residues in accordance with the experimental conditions of pH 7.4 as used in ref 29, we utilized an empirical pK_a predictor available in the PROPKA3 program.[58] Based on this pK_a analysis, we considered two histidine residues—His67 and His247 in subdomains IA and IIA, respectively—to be protonated at both Nδ and Nε positions. Neutral states for all other histidines of HSA were assumed with proton attached to the Nε position. All aspartate and glutamate residues were considered to be deprotonated, while all arginines and lysines were assumed to be positively charged. An exception here is the Lys199 for which the neutral form was adopted in the simulations of AY or PF^+ at BS1. The neutral form of Lys199 was proposed by Díaz et al.[59] based on the restrained MD studies of Lys195 and Lys199 protonation states. This choice is also supported by the low Lys199 pK_a value of 7.4 predicted using the PROPKA3 program which agrees well with the experimental value[1,59] of around 8, and furthermore a detailed analysis of the local structure of the protein around AY at BS1 indicates a possibility of hydrogen bonding between one of the amino groups of AY and Nζ atom of neutral Lys199 acting as hydrogen bond acceptor. The Amber99SB force field[60] was used to model albumin in the simulations. The combined charge of HSA (−12, or −13 in the case of neutral Lys199) and the ligand (0 for AY and +1 for PF^+) was neutralized by adding an appropriate number of Na^+ counterions. The Antechamber module of Amber11 was used to assign atomic types and corresponding force field parameters to the atoms of the ligand and the protein.

Molecular systems consisting of a single AY^+ or PF^+ chromophore in aqueous solution represented by more than 6000 TIP3P water molecules along with a single neutralizing Cl^- counterion were initialized in a rectangular box using the Antechamber module of Amber11. MD simulations were performed using the Sander module of Amber11.[44] The time step of 1 fs was chosen for the leapfrog integrator. Pairwise electrostatic and Lennard-Jones interactions were cut at 10 Å, and periodic boundary conditions were employed. Water molecules were subject to bond length and angle constraints using the SETTLE scheme.[61] A short initial 50 ps long NVT simulation at a temperature of 30 K was conducted in order to remove any possible bad contacts. The temperature was controlled using the Langevin thermostat with the collision frequency of 3.0 ps^{-1}. Then, a 300 ps long NPT simulation at the pressure of 1 bar with a gradual increase of temperature from 30 to 297 K followed in order to obtain the correct density of the system corresponding to chosen conditions. Finally, we switched back to the NVT ensemble at 297 K to perform a 500 ps long equilibration followed by 1 ns long production run. Molecular snapshots were taken every 250 fs to be used in the subsequent analysis, and a set of 100 molecular configurations spaced at regular intervals of 10 ps was selected to be used in the PE-DFT calculations of excitation energies.

Having to consider two ligands and three binding sites, we performed six distinct MD simulations of each individual ligand−HSA complex. Each system along with the neutralizing counterions was solvated by a rectangular box of more than 32 000 TIP3P water molecules. Initial location of the ligand at the binding site at hand was determined based on the results of docking simulations described below. The integration step of 2 fs and the nonbonded cutoff of 8 Å were utilized in these simulations, and all other MD settings were kept the same as used in the simulations of aqueous chromophores. The system was first subject to steepest descent molecular mechanical minimization with all heavy atoms restrained to their initial positions. Subsequently, a short 20 ps long NPT simulation at the temperature of 297 K and pressure of 1 bar was conducted keeping restraints on the heavy atoms. Geometrical restraints were removed in the following simulations. However, bond length constraints involving hydrogen atoms were imposed for the protein atoms using SHAKE,[62] and rigidity of the water molecules was enforced using SETTLE. A 200 ps NPT simulation at the temperature of 297 K and pressure of 1 bar was given for the system to reach the appropriate density. The system was then allowed to evolve for 5 ns in the NVT ensemble, and the trajectory was recorded every 1 ps to be used for analysis as well as in the PE-DFT calculations.

B. Electronic Structure Calculations. To model photoabsorption spectra, we rely on the vertical electronic excitation energies provided by the linear response time-dependent DFT approach[63,64] where the transition energies and associated transition dipole moments are defined as poles and residues, respectively, of the electric dipole−dipole linear response function. In the polarizable embedding DFT scheme,[37,38] the static charge density distribution of the classical region is generally approximated by localized permanent electric multipole moment expansions. The polarization of the classical region is generally introduced through a set of anisotropic polarizabilities localized typically on the atomic centers of the classical region which gives rise to induced dipole moments. The self-consistency between the electronic density of the quantum region and induced dipoles of the classical region is achieved by solving effective Kohn−Sham equations, and induction interactions are thus accounted for in an explicit manner. The response properties depend not only on the polarized electronic density of the quantum region implicitly but there is also an explicit contribution to the response function originating from the electronic density dependence of the polarizable embedding potential in the Kohn−Sham Hamiltonian. The linear and quadratic response time-dependent PE-DFT model has been implemented in the development version of the Dalton quantum chemistry program.[65]

We used the CAM-B3LYP exchange-correlation functional[66] in its original parametrization in combination with the Dunning's aug-cc-pVDZ basis set[53] for all excitation energy calculations in this work. The CAM-B3LYP functional provides accurate vertical excitation energies in both gas and condensed phases.[67−69] Our test calculations on isolated geometry-optimized AY, AY^+, and PF^+ chromophores showed that the lowest excitation energies are converged to within 0.01 eV as compared to the results obtained using more extensive daug-cc-pVTZ basis set. Vacuum geometries of the chromophores were optimized at the B3LYP/cc-pVTZ level using Gaussian09.

We applied periodic boundary conditions for every molecular configuration taken from the MD trajectory in order to center the chromophore in the middle of the rectangular box. Our test calculations revealed that around 370 water molecules distributed spherically around the solute offers a sufficient representation of the aqueous medium giving well-converged excitation energies. In the PE-DFT calculations within the aqueous solution, the quantum region comprises the chromophore or the chromophore plus a few nearest solvent

dx.doi.org/10.1021/jp311863x | J. Phys. Chem. B 2013, 117, 2069−2080

molecules. In the latter case, the model goes beyond the classical electrostatic-induction picture and allows us to assess the importance of nonelectrostatic effects. The induced dipole moments of the water molecules were determined using the relay matrix procedure.

We included 1000 nearest water molecules around the chromophore in the response calculations within the protein environment. The Na^+ counterions were found to be located too far away from the ligand to have any considerable impact and were discarded. HSA and all water molecules were described by a classical embedding potential, while the chromophore alone was treated using DFT. Induced dipole moments of the protein and water molecules were calculated using an iterative scheme due to the large number of polarizable centers present in the classical region in this case.

Due to the presence of two nearby electronic excited states of both neutral and cationic forms of the dye molecules, the statistical mean of the excitation energy taken over the set of molecular configurations is not a suitable approximation of the maximum absorption energy measured in the condensed phase. Therefore, we constructed the absorption spectrum of the chromophore in condensed phase by assigning a Gaussian contour to each individual electronic transition of energy, E_i^{exc}, and oscillator strength, f_i, according to

$$A(E) = \frac{28700}{\sqrt{\sigma}} \sum_i f_i \exp\left[-\left(\frac{E - E_i^{\mathrm{exc}}}{2\sigma}\right)^2\right] \quad (1)$$

In this equation, A is the absorbance which is a function of the energy of the photons, E, and σ is an empirical broadening parameter. The summation runs over the two lowest electronic transitions in the set of molecular configurations taken from the MD simulation. The energy corresponding to the peak intensity of the resulting absorption spectrum is our approximation to that recorded experimentally. Our test calculations showed a relatively rapid convergence of the maximum intensity excitation energy so that around 80 configurations are sufficient to obtain statistical convergence up to 0.01 eV. The broadening parameter σ was set to 0.2 eV, and we have seen the results for the energy of the maximum absorption to be virtually insensitive to σ in the range of 0.1 to 0.4 eV. Length-gauge oscillator strengths were used in eq 1.

C. Classical Potentials. In the PE-DFT calculations, we utilized both nonpolarizable and polarizable embedding potentials for the HSA protein and water molecules. The point charges of the nonpolarizable potential for albumin were taken from the Amber99SB force field, and thus the polarization of the protein is modeled implicitly. The classical embedding potentials used in the PE-DFT calculations consisted of atomic point charges fitted to reproduce the electrostatic potential calculated at B3LYP/cc-pVTZ level using Gaussian 09.[47] The fitting was performed using the RESP procedure[50] as implemented in the Antechamber[51] program of the AmberTools 11[44] program package. The point charges represent the permanent charge distribution of the environment. To model the induced potential, we calculated localized electronic isotropic dipole−dipole polarizabilities. These were computed using the localized properties (LoProp)[70] procedure implemented in Molcas[71] with B3LYP and an atomic natural orbital (ANO) type recontraction of the 6-31+G* basis set. The resulting polarizable embedding potential is designated resp-p1.

To derive the properties entering the classical embedding potentials of the protein we used the molecular fractionation with conjugate caps method[39] to decompose it into smaller amino acid-based fragments. Here we fragmented the full protein into amino acid residues capped with $COCH_3$ and $NHCH_3$ groups built using atoms from neighboring residues. In addition to the capped amino acid fragments, two neighboring $COCH_3$ and $NHCH_3$ capping groups are merged to form *N*-methylacetamide (NMA), a so-called concap. The purpose of the NMAs is to remove the double counting from using overlapping fragments as well as emulating the immediate environment surrounding the amino acids. In the case of disulfide bonds we used SCH_3 capping groups. Originally, this approach was used to calculate ligand−protein interaction energies[39] by summing the interaction energies between the ligand and the capped amino acid fragments and subtracting the interaction energies between the ligand and the cap fragments. Here it was used to derive the embedding potential in a similar manner.[72] Thus, we decomposed the protein into capped amino acid fragments and the corresponding concaps, calculated the properties of all fragments individually, and finally used the same principle as for the interaction energy to obtain the embedding potential of the whole system. Accordingly, an atom-centered property P on atom A is calculated as

$$P^{\mathrm{A}} = \sum_{f=1}^{F} P_f^A - \sum_{c=1}^{C} P_c^{\mathrm{A}} \quad (2)$$

where P_f^A is the property on atom A in the fth amino acid fragment and P_c^A is the property on atom A in the cth concap. F and C are the number of capped amino acid fragments and concaps, respectively, that contain atom A.

Three different potentials were used to represent water molecules. They include the nonpolarizable TIP3P as well as polarizable potentials due to Ahlström et al.[73] and the resp-p1 potential. The latter is based on the RESP fitting of the point charges and LoProp calculations of distributed atomic dipole−dipole polarizabilities in the same manner as for the albumin protein. The parameters used for water molecules are collected in Table 1.

Table 1. Water Potential Parameters Used in the PE-DFT Calculations: Partial Point Charges, q, and Isotropic Polarizabilities, α, All in au

potential	q(O)	q(H)	α(O)	α(H)
TIP3P	−0.834000	0.417000	–	–
resp-p1	−0.698472	0.349236	4.3086	1.2260
Ahlström	−0.669000	0.334500	9.7180	0.0000

D. Docking. Molecular docking was conducted using the AutoDock Vina[74] program, and AutoDock Tools[75] was used for input preparation. AutoDock Vina belongs to the class of the molecular docking software which utilizes a machine-learning type of the scoring function rather than one based on physical quantities. The structure of the receptor from pdb id 1N5U was used after all ligands and water molecules were removed. Hydrogen atoms were added to the electronegative atoms of albumin according to default routines of AutoDock Tools. The structure of both albumin and the ligand were kept rigid during the docking run apart from the two amino groups of AY or PF^+ which were allowed to rotate. Docking simulations were

dx.doi.org/10.1021/jp311863x | J. Phys. Chem. B 2013, 117, 2069−2080

performed for both ligands at each of the considered binding sites separately, so that the search space was confined only to the specific binding site at hand. Blind docking was also performed in order to find high-affinity binding sites of HSA for the two ligands, and the search space included the entire receptor in this case.

III. RESULTS AND DISCUSSION

A. Photoabsorption in Gas Phase and Aqueous Solution. The two lowest $\pi\pi^*$ electronic excitation energies of the AY, AY^+, and PF^+ chromophores computed in vacuum are collected in Table 2. Higher electronic states with substantial oscillator strengths for the vertical excitations are located around 4.8 and more than 5 eV above the ground state of, respectively, neutral AY and protonated forms of AY^+ and PF^+, and are thus well separated from the two lowest excited states. The linear response DFT thus predicts that the lowest absorption bands of AY and PF dyes hide two electronic transitions, although only one of them is expected to be significant due to its much higher oscillator strength as compared to the other (Table 2). We will therefore focus on the two lowest electronic transitions of the chromophores in the rest of the paper.

Table 2. Two Lowest Excitation Energies (in eV) of AY, AY^+, and PF^+ Molecules Calculated using CAM-B3LYP/aug-cc-pVDZ Method in Vacuum[a]

	AY	AY^+	PF^+
HOMO−LUMO	3.50 (0.03)	3.35 (0.77)	3.38 (0.70)
HOMO-1−LUMO	3.70 (0.33)	3.55 (0.01)	3.63 (0.01)

[a]The corresponding length-gauge oscillator strengths are given in parentheses.

The analysis of the DFT-based response vector shows that the lowest excitation is dominated by the HOMO−LUMO transition, whereas the second lowest is dominated by the HOMO-1−LUMO transition. The frontier Kohn−Sham molecular orbitals of AY and AY^+ are depicted in Figure 3. The corresponding Kohn−Sham orbitals of PF^+ have virtually the same shape as those of AY^+. As seen in Figure 3, the HOMO and HOMO-1 of protonated AY^+ interchange their relative positions in the energy ordering of the Kohn−Sham orbitals as compared to the neutral AY form. This has immediate consequences for the photoabsorption of the two forms of AY as the "bright" state being the second lowest in neutral AY becomes the first in the protonated AY^+ (see Table 2). The protonation of AY leads to the reduced magnitude of the intense electronic transition energy by −0.35 eV which happens to agree very well with the corresponding shift of 0.36 eV recorded for the absorption band due to the deprotonation of PF^+ in basic aqueous solution.[32] This suggests that differential solvation effects on the experimentally measured shift might likely be of secondary importance. The hypochromic effect seen upon deprotonation of PF^+ in aqueous solution[32] is also qualitatively well reproduced by the calculations in vacuum. The methyl groups in AY^+ are indeed seen to have a rather small effect on the excitation energy to the "bright" electronic state, reducing it by only 0.03 eV compared to methyl-free PF^+, in line with the experimentally observed maximum absorption at the same wavelength of both PF^+ and AY^+ in aqueous solution.

We have collected the results for the maximum absorption energies of aqueous AY^+ and PF^+ based on PE-DFT calculations using different solvent models in Table 3. First,

Table 3. PE-DFT-Based Peak-Intensity Absorption Energies (in eV) of AY^+ and PF^+ Dyes in Aqueous Solution Computed Using Eq 1 for 100 Solute-Solvent Configurations[a]

potential	no. $(H_2O)_{qm}$	AY^+	PF^+
in vacuum	–	3.28	3.35
TIP3P	0	3.30	3.39
resp-p1	0	3.24	3.33
Ahlström	0	3.22	3.30
resp-p1	4[b]	3.24	3.32
resp-p1	5[c]	3.23	3.31
expt		2.82[d]	2.79,[e] 2.82[d]

[a]Excitation energies are based on CAM-B3LYP/aug-cc-pVDZ calculations along with the potential for water molecules given in the first column. Second column indicates the number of water molecules treated quantum mechanically. [b]One water molecule closest to each of the 4 meta and ortho carbon atoms in the central ring. [c]One water molecule closest to each of the 5 H atoms connected to nitrogen. [d]Reference 29. [e]References 30 and 32.

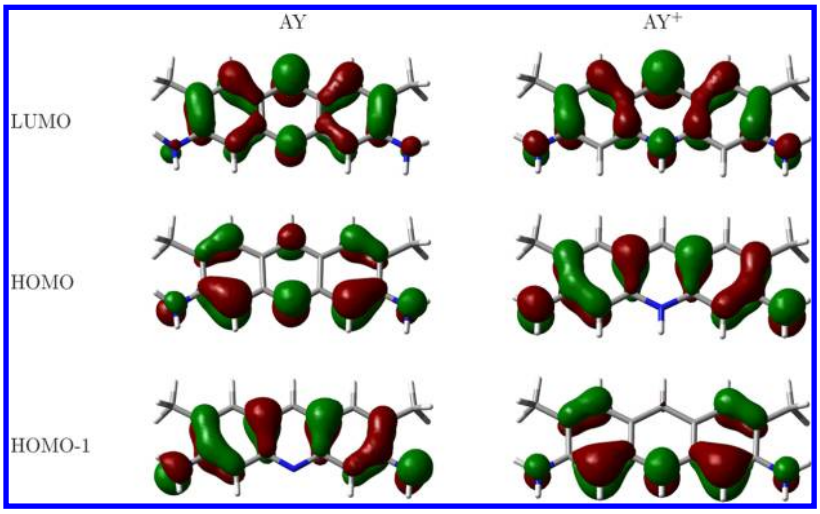

Figure 3. Surface representation of some frontier Kohn−Sham molecular orbitals of AY and AY^+ based on B3LYP/cc-pVTZ.

dx.doi.org/10.1021/jp311863x | J. Phys. Chem. B 2013, 117, 2069−2080

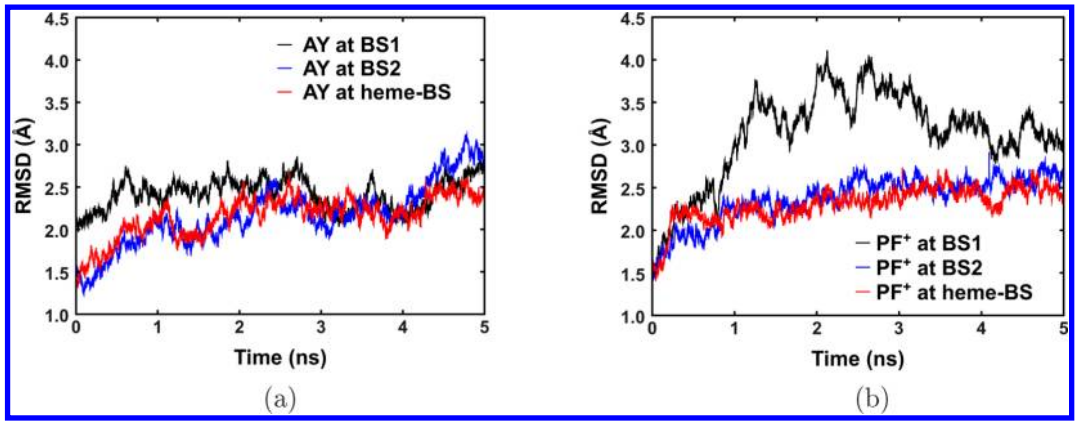

Figure 4. HSA backbone C−Cα−N RMSD from the crystal structure (pdb id 1N5U) as a function of the 5 ns NVT MD simulation of AY (a) and PF^+ (b) at BS1, BS2, and heme-BS.

we calculated the vertical excitation energies for the liquid-phase geometries of AY^+ and PF^+ as recorded during the MD simulations but with all solvent molecules removed. Compared to the high oscillator strength excitation energies of the cationic dyes computed in vacuum (Table 2), we can see in Table 3 that intramolecular vibrational dynamics of the chromophores in solution has a red-shifting effect on the maximum absorption energy which is somewhat more pronounced for AY^+ than for PF^+. Interestingly, the electrostatic and implicit polarization interactions modeled by using the point-charge-based TIP3P potential for water molecules have an opposite blue-shifting effect. These two effects happen to virtually cancel each other in the case of PF^+. The explicit treatment of solute−solvent induction via the polarizable resp-p1 or Ahlström potentials is seen to cause a red shift in the maximum absorption energy of the two chromophores in water solution. Explicit polarization interactions are thus not only seen to shift the maximum absorption energy to the different direction as compared to the pairwise electrostatics but also the magnitude of the shift is larger roughly by a factor of 2. It is thereby mandatory to account for polarization interactions explicitly by using a polarizable embedding potential in order to obtain a physically correct picture of the photoabsorption processes in these chromophores in the condensed phase.

Among the two polarizable water potentials used in this work, the Ahlström potential should be considered superior over the resp-p1. The atomic point charges included in the Ahlström potential reproduce the electric dipole moment of the water molecule in the gas phase (1.86 D), and the polarizability of around 9.7 au agrees well with the high-level coupled cluster CCSD/aug-cc-pVQZ predictions and experimental results.[76] The resp-p1 type of potential adopted in this work for water molecules suffers from evidently underestimated atomic polarizabilities. The net isotropic polarizability of resp-p1 water molecule amounts to only around 6.7 au (Table 1). This is primarily related to the modest basis set used in the LoProp calculation as rather severe basis set requirements for molecular polarizabilities are well-documented.[77,78] Especially important are the diffuse functions which are only added to non-hydrogen atoms in the basis set used. Therefore, this issue will be less pronounced for the protein resp-p1 embedding potential. Furthermore, the resp-p1 potential for the water molecules includes point charges which are larger in magnitude as compared to those of the Ahlström potential meaning that part of the missing polarization in the condensed phase is recovered by the larger permanent dipole moment. As it is evident from the results in Table 3, the difference between the maximum absorption energies of AY^+ and PF^+ in water solution calculated using the two water potentials is only 0.02−0.03 eV. This is indeed an acceptable accuracy for the purposes of the current work.

In order to go beyond the electrostatic-induction picture in the PE-DFT excitation energy calculations on aqueous AY^+ and PF^+, we refined the model by including some of the potentially important water molecules along with the solute to the quantum mechanically described region. In addition to the improved description of the electrostatic and induction interactions, such a scheme allows us to account for nonelectrostatic effects, primarily short-range repulsion since dispersion interactions is a well-known bottleneck of standard DFT methods.[79,80] Previously, it has been found that nonelectrostatic interactions with hydrogen bonding as well as delocalized π system attacking solvent molecules can account for roughly half of the solvent shift in the $\pi\pi^*$ excitation energy.[69] We have therefore performed two series of PE-DFT calculations on both chromophores in aqueous solution where we include (a) 4 water molecules above or below the molecular plane of the chromophore and (b) 5 water molecules potentially forming hydrogen bonds with the H−N bonds of AY^+ and PF^+ acting as hydrogen bond donors. The results included in Table 3 somewhat unexpectedly reveal that the maximum absorption energy of both AY^+ and PF^+ in aqueous solution is virtually insensitive to the quantum mechanical description of the water molecules. This brings in some optimism that it might be indeed an acceptable approximation to neglect nonelectrostatic effects in the PE-DFT calculations of the photoabsorption of these cationic dyes within the protein environment as well.

The computed maximum absorption energies of AY^+ and PF^+ in water solution differ by around 0.1 eV (Table 3). This is primarily due to the differential geometrical effects, whereas the direct solvent effect on the solvatochromic shift is indeed of similar magnitude for both chromophores. The absolute magnitude of the computed maximum absorption energy of aqueous chromophores is overestimated by around 0.4−0.5 eV as compared to the experimental observations. This is, however, within the limits of expected accuracy of the DFT methods in predictions of vertical excitation energies.[81,82] The differences between the absorption energies are expected to be considerably more accurate thanks to error cancellation.

dx.doi.org/10.1021/jp311863x | J. Phys. Chem. B 2013, 117, 2069−2080

B. AY and PF^+ Bound to HSA: Structural Results. Our first-choice candidate sites to bind the AY and PF^+ chromophores were the two primary drug binding sites BS1 and BS2 of HSA. Our blind docking simulations have shown, however, that the highest affinity binding site for both ligands is that of heme-BS with −10.0 and −10.4 kcal/mol affinity for AY and PF^+, respectively. The other high-affinity binding sites happen to be BS2 (−8.9 and −9.0 kcal/mol affinity for AY and PF^+, respectively) and a fatty acid binding site no. 2 in subdomain IA (−9.4 and −8.9 kcal/mol affinity for AY and PF^+, respectively), according to the nomenclature given in refs 3, 6, and 25. Although the high affinity of heme-BS toward the two ligands is likely biased because of the empty gap originally filled by heme in the measured crystal structure of HSA, we decided to take this site into consideration as well. Compared to heme-BS and BS2, the lower affinities for AY and PF^+ binding at BS1 of −8.2 and −7.4 kcal/mol, respectively, were found.

We performed docking simulations for both ligands at each of the three binding sites separately, and the search space was confined to solely the specific binding site at hand. The resulting highest-affinity ligand−HSA configurations were used as a starting point for the six individual MD runs. In Figure 4, we show the root-mean-square deviations (rmsd) of the HSA backbone atoms from the crystal structure recorded during the last 5 ns of our NVT simulations. The rmsd is seen to reach a relatively constant value after around 2 ns of the MD simulation, in line with the findings reported in refs 33−36. The last 3 ns of the simulation are thereby considered as the production run. We can see that AY induces very similar deviations of the simulated HSA structure as compared to the crystal structure of the protein, irrespective of the binding site the ligand has docked at. The same statement is also valid in the case of PF^+ bound at BS2 and heme-BS. Somewhat larger deviations from the crystal structure were, however, seen for cationic PF^+ bound at BS1. The overall drift of the simulated structure of HSA from its crystal structure is rather small, and in fact very similar to that seen in the MD simulations[35] of unliganded HSA starting from the same crystal structure as in current study. The α-helix content in HSA was seen to be very similar for both ligands, around 60% for AY and around 56% for PF^+, at any of the considered binding sites. The circular dichroism measurements of ref 29 have shown an indication of AY inducing a prominent reduction of α-helical content in HSA by more than 20% compared to the unliganded protein, whereas PF^+ did not impart any substantial changes to the secondary structure of HSA. Our simulations thus do not reproduce this finding. We note, however, that reservations of circular dichroism spectroscopy to provide insight into the secondary structure of proteins have recently been discussed.[6,83]

The three considered binding sites of HSA are depicted in Figure 1, and the local microenvironment of the AY and PF^+ chromophores bound at each of the three sites as recorded during the NVT production run is shown in Figures 5 and 6, respectively. Within the BS1, the AY chromophore has found its place at the inner side of the doorway region to the binding site represented by the positively charged residues Arg218, Arg222, and Lys195 as well as Lys199 which we have treated in its neutral form; see Figure 5a. The chromophore's central N atom and the amino group in the vicinity of Lys199 and His242 are strongly involved in the hydrogen bonding with water molecules. The other amino group is found to be in close

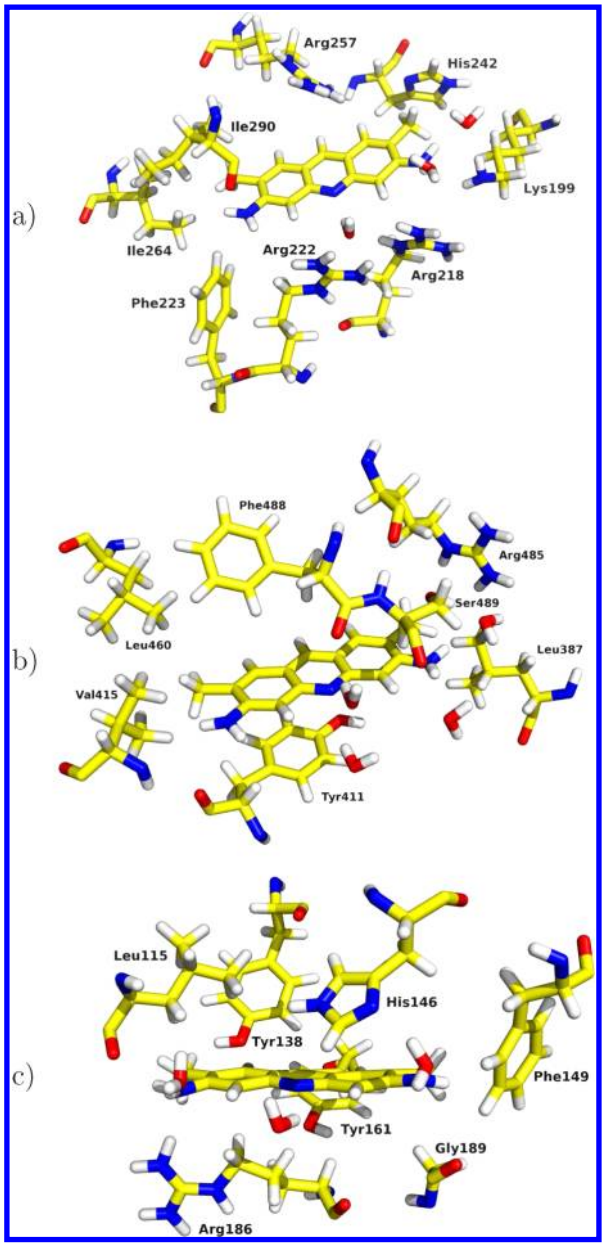

Figure 5. Nearest surroundings of AY bound at BS1 (a), BS2 (b), and heme-BS (c).

contact with the protein's backbone O atom of Ile290. The apolar edge of AY is facing the hydrophobic region of BS1 formed from apolar residues such as Leu238, Leu260, Ile264, Ile290, and Ala291. The Arg257 residue is seen to be located above the plane of AY.

The AY chromophore is found at the entrance region of BS2 as well; see Figure 5b. The central nitrogen atom and one of the amino groups are thus exposed to hydrogen bonding with water molecules. In addition, the hydroxyl group of Ser489 is found to attack the latter amino group as well. The side chain of the Tyr410 residue is found to be on a side of the AY's molecular plane where the hydroxyl group is located in the vicinity of the central N atom, and the backbone O atom of Tyr410 is involved in the hydrogen bonding with the solvent-screened amino group of AY. The presence of Phe488 residue is seen on the other side of the AY's molecular plane. Besides Arg485 next to the water exposed end of AY, apolar residues of HSA, e.g.,

dx.doi.org/10.1021/jp311863x | J. Phys. Chem. B 2013, 117, 2069−2080

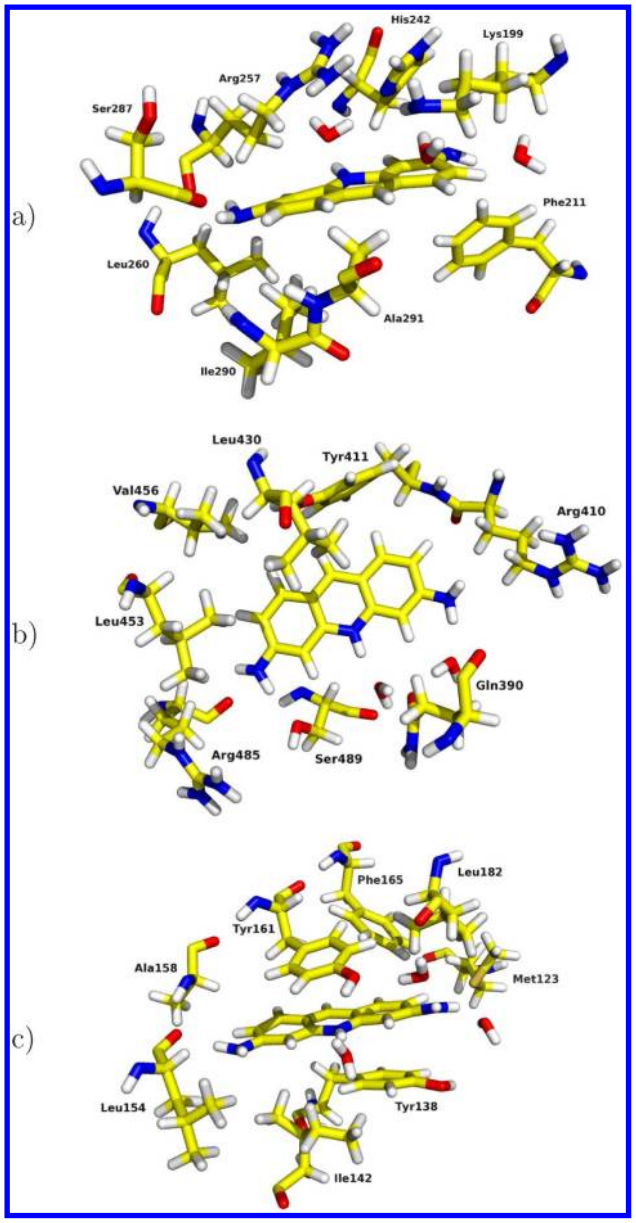

Figure 6. Nearest surroundings of PF^+ bound at BS1 (a), BS2 (b), and heme-BS (c).

Leu423, Leu387, Leu453, Leu460, Val415, Val420, and Val456, are found to be in contact with the hydrophobic edge of AY.

Although docking simulations have predicted the position of AY to be in-between the side chains of the residues Tyr138 and Tyr161 at heme-BS, the chromophore escapes this configuration on the course of simulation leaving the two Tyr residues behind its hydrophobic edge; see Figure 5c. Among the three considered binding sites, AY is most heavily exposed to water in the heme-BS. The His146 residue is always seen to be in the vicinity of AY. The binding pattern of AY is seen to slightly change after around halfway of our production run. For example, the backbone O atom of Leu115 is seen to be in close contact with one of the amino groups of AY, but after 3.5 ns of simulation this residue moves further away. In contrast, the backbone O atom of Gly189 shows small and stable distance to the other amino group throughout the simulation, and the hydroxyl group of Ser193 was seen to be in the vicinity of this group as well. The microenvironment of AY at heme-BS is found to be inhomogeneous as in the other two binding sites as it is composed of both the aliphatic apolar residues Leu115, Leu182, Val116, and Ile142 as well as polar or polarizable residues Ser192, Ser193, Arg186, Phe149, and Phe157.

The PF^+ chromophore is found to be situated in a similar location within BS1 like AY, but it does adopt a different orientation; see Figure 6a. Even though the hydrophilic edge of the ligand is facing the hydrophobic wall of BS1 represented by residues Leu203, Leu238, Val241, Leu260, Ala258, and Ala261, the central N atom and one of the amino groups are involved in the hydrogen bonding with water molecules which have penetrated into the interior of BS1. The other amino group is seen to be hydrogen bonded to the two backbone O atoms of the Arg257 and Ser287 residues. The side chains of Arg257 and His242 are found to be located on the same side of chromophore's molecular plane.

Like in the case of AY, the PF^+ chromophore is half-inside of BS2, so that the central N atom and one amino group are available for hydrogen bonding with water; see Figure 6b. The Arg410 residue is always seen to be in the vicinity of this water-exposed amino group of PF^+. The other amino group is in turn involved in hydrogen bonding with the backbone O atom of Arg485 and hydroxyl group of Ser489. The polar side chain of Gln390 is seen to be in the vicinity of the hydrophilic edge of the chromophore as well. Tyr411 together with apolar residues Leu407, Leu430, Leu453, Leu457, Leu460, and Val426 are seen to be in contact with the hydrophobic edge of the PF^+ chromophore.

In contrast to AY, PF^+ chromophore was seen to remain sandwiched between the Tyr138 and Tyr161 residues within the heme-BS throughout the entire MD simulation; see Figure 6c. The hydrophilic edge of the chromophore is strongly exposed to the water solution where hydrogen bonds are constantly formed. The only exception is a backbone O atom of Leu153 which is involved in the hydrogen bonding with one of the amino groups of PF^+.

C. AY and PF^+ Bound to HSA: Photoabsorption. Our test calculations showed that a set of 80 molecular configurations is a sufficiently large representation of the ligand−protein phase space to obtain converged maximum absorption energies using eq 1. Configurations used in the PE-DFT calculations were selected at regular intervals of 25 ps from each of the trajectory, and it is expected that they are statistically uncorrelated and bring in statistically significant information. We used two different classical representations of the protein and water molecules in the PE-DFT calculations of excitation energies. First, we utilized parameters as used in the MD simulation, that is, partial point charges from the Amber99SB force field for HSA protein and from TIP3P for water molecules. The second approach was to use a polarizable embedding potential based on partial point charges fitted to reproduce quantum mechanical electrostatic potentials and LoProp calculations of atomic polarizabilities for every individual residue of the protein as described in section IIC. Due to the high computational costs of such a scheme, the potential parameters were derived for only one geometry of the protein randomly chosen from each of the six sets of molecular ligand−protein configurations. The derived embedding potential for the protein was then used in every molecular configuration within the specific set. In this way, we accounted for the potentially different structure and therefore the embedding potential of the binding site depending on the presence or the absence of the ligand. Apart from this, we

dx.doi.org/10.1021/jp311863x | J. Phys. Chem. B 2013, 117, 2069−2080

Table 4. PE-DFT-Based Peak-Intensity Absorption Energies (in eV) of AY and PF^+ Dyes Bound to Different Sites within HSA Computed Using Eq 1 for 80 Molecular Configurations[a]

ligand	potential	BS1	BS2	heme-BS	expt.
AY	Amber99SB/TIP3P	3.46 (0.16)	3.44 (0.14)	3.44 (0.14)	3.15 (0.33)
	resp-p1	3.39 (0.15)	3.36 (0.12)	3.36 (0.12)	
PF^+	Amber99SB/TIP3P	3.22 (−0.17)	3.30 (−0.09)	3.28 (−0.11)	2.79 (−0.03)
	resp-p1	3.14 (−0.19)	3.25 (−0.08)	3.14 (−0.19)	

[a]The shifts of the peak-intensity absorption energies (in eV) with respect to those computed for AY^+ and PF^+ chromophores in aqueous solution using the respective potentials for water molecules are given in parentheses. Excitation energies are based on CAM-B3LYP/aug-cc-pVDZ calculations along with the potential for the protein and water molecules given in the second column. Experimental data taken from ref 29.

assumed conformational or more generally structural independence of the embedding potential parameters. Instead of using some standard polarizable embedding potential for water molecules in the PE-DFT calculations, we adopted exactly the same procedure to derive the potential on the equilibrium TIP3P geometry of the molecule as for the protein in order to preserve consistency of the computational approach.

We have collected the predicted peak-intensity absorption energies of the two chromophores bound to the HSA protein in Table 4, where we also evaluated the solvatochromic effect induced by the protein environment with respect to the chromophore's absorption in pure aqueous solution. The evaluated aqueous solution-to-protein environment shifts for AY chromophore are seen to be virtually independent of the binding site. In addition, the shifts obtained using the Amber99SB/TIP3P based point charge embedding potential are similar to those obtained using the more advanced polarizable resp-p1 potential. Thereby, we can see that the effect of explicit polarization interactions, although important for the absolute magnitude of the maximum absorption energy in the condensed phase, tends to cancel in the calculation of the aqueous solution-to-protein shift. The predicted shift amounts to 36−48% of the experimentally measured 0.33 eV. The achieved results thus do not allow to draw conclusions on a preferred binding site of AY within HSA. The calculations also indicate UV absorption to be blind in discriminating the possible selective binding of AY chromophore at any of the considered binding sites of HSA.

The calculated shifts for PF^+ chromophore bound at BS1 and BS2 are again similar and independent of the quality of the used embedding potential. A prominent effect of an explicit treatment of the polarization interactions is, however, seen in the case of PF^+ bound to heme-BS, where a considerable increase in the magnitude of the shift by around 70% is observed. This finding is likely related to the fact that the PF^+ chromophore is situated between the side chains of the Tyr138 and Tyr161 residues in a parallel configuration, an arrangement which is absent in any other of the considered systems. A very small shift of around −0.03 eV was recorded for PF^+ experimentally, the magnitude of which is significantly overestimated in the cases of PF^+ bound at BS1 and heme-BS. Our calculations are expected to be of sufficiently high predictive quality to allow us to conclude that the cationic PF^+ chromophore does not bind to HSA at these two binding sites. Among the considered binding sites, BS2 alone could be subject to a more careful scrutiny as a potential binding site for the PF^+ dye molecule within HSA.

A rather poor quantitative agreement between the computed and experimental results for the shifts of maximum absorption energies going from aqueous solution to protein environment generally suggests some inherent deficiencies in the modeling scheme we have adopted to tackle the problem. First of all, we have neglected the conformational dependence of the embedding potential parameters. This is a well-known issue in classical MD simulations[84] but is likely to be equally severe in the PE-DFT calculations, where the quality of the results strongly depends on how accurately the electrostatic potential is reproduced by the embedding potential within the volume of the quantum mechanically described region. Conformational dependence of isotropic polarizabilities has recently been shown to be significant as well.[85] Another deficiency of the currently used polarizabilities is related to the rather small basis used to compute them; in fact, basis sets as large as aug-cc-pVTZ have been recommended for LoProp calculations of polarizabilities.[85] To obtain an improved description of electrostatic as well as induction interactions, the embedding potential used in the PE-DFT calculations could potentially include higher permanent multipole moments especially up to at least quadrupoles[86] as well as anisotropic polarizabilities. Although we found nonelectrostatic effects to be insignificant for the computed excitation energies of the chromophores in aqueous solution, they might be more important within the inhomogeneous protein environment where both hydrophobic and charged residues are in contact with the ligand simultaneously. A refinement of the computational model along the lines discussed above is unfortunately not feasible for the computational resources currently available.

Another potentially significant source of error is related to the imperfections of the force field used in the MD simulations. The widely accepted and used dynamical averaging scheme where a condensed-phase property is evaluated as an average over the properties calculated for a set of snapshots taken from the *classical* MD simulations is known to generally fail in the predictions of the nuclear magnetic resonance (NMR) spectra.[87] The reason lies in the inaccurate sampling of the vibrational phase space of the sample which is due to the limitations of the force field used in the MD simulations.[88] Obviously, this failure is inherent in the PE-DFT-based excitation energies as well. For example, we computed the maximum intensity absorption energy of PF^+ at BS3 of HSA in vacuum, i.e., with the entire environment neglected. The resulting absorption energy is 3.30 eV and should be compared to that of 3.35 eV predicted in vacuum for the chromophore's geometries sampled in aqueous solution (Table 3). Clearly, differential geometrical effects in the calculation of the shift are indeed important.

IV. SUMMARY AND CONCLUDING REMARKS

In this pilot computational study, we attempted to scrutinize the curious solvatochromic behavior of AY and PF^+ cationic dye molecules upon binding to the human serum albumin (HSA) protein. We considered three binding sites of albumin,

primary drug binding sites 1 and 2 as well as a heme binding site, as possible candidates to adopt AY and PF^+ chromophores. Extensive nanosecond-scale classical MD simulations of the two chromophores in aqueous solution as well as within the protein were conducted. Molecular configurations generated during the MD simulations were subject to large-scale linear response PE-DFT calculations of vertical excitation energies. We utilized an advanced polarizable embedding potential for the protein based on electrostatic potential fitted point charges and LoProp atomic polarizabilities calculated for individual residues of the partitioned protein. Peak-intensity absorption energies of the chromophores in condensed phase were determined by assigning a Gaussian absorption contour with an empirical broadening for every individual vertical transition.

The calculated aqueous solution-to-protein environment shift of the maximum intensity absorption energy of PF^+ is −0.19 eV when the chromophore is bound at BS1 and heme-BS of HSA. The magnitude of the shift is considerably overestimated as compared to experimentally measured shift of −0.03 eV, leading to the conclusion that the cationic PF^+ chromophore likely does not bind any of the two sites. This confirms the assumption that cationic ligands should not bind to HSA, in particular at BS1. Considering the heterogeneous nature of the considered binding sites which leads to a rather large shift, it is indeed likely that the PF^+ chromophore might find its location on the water-exposed surface of the HSA protein. A very similar shift of around 0.12−0.15 eV for maximum absorption of AY at the three considered binding sites was obtained which thus is underestimated as compared to experimental shift of 0.33 eV.

Although quantitative agreement with experimental shifts is not obtained—probably owing to limitations of the embedding potential used for the protein in the PE-DFT calculations—the trends in the shifts are qualitatively correct, and likewise so the differential shift between the two chromophores. We find the latter to be due to that AY binds HSA in its neutral deprotonated form, whereas PF^+ retains its cationic state while interacting with the protein. Thus, the degree of deprotonation might be the crucial factor for optical probing of systems like the one studied here rather than the actual site of binding to the protein. This specific result is in line with more general conclusions that indirect chromophore reconformation may be just as important for the action of an optical probe, specifically its solvatochromic shift, as the direct environmental, herein protein, perturbation of its electronic structure and spectrum.[43,89] This in turn has ramifications for the design of flexible chromophores that are optimal for protein probing.

AUTHOR INFORMATION

Corresponding Author

*E-mail: kestutis.aidas@ff.vu.lt.

Notes

The authors declare no competing financial interest.

ACKNOWLEDGMENTS

This work was supported by the grants from the Swedish Infrastructure Committee (SNIC) for the projects "Multi-physics Modeling of Molecular Materials", SNIC 023/07-18. J.K. thanks The Danish Councils for Independent Research (STENO and Sapere Aude programmes), the Lundbeck Foundation, and the Villum Foundation for financial support. Postdoctoral fellowship to K.A. is being funded by European Union Structural Funds project "Postdoctoral Fellowship Implementation in Lithuania".

REFERENCES

(1) Peters, Jr., T. *All about Albumin: Biochemistry, Genetics, and Medical Applications*; Academic Press: San Diego, CA, 1996.

(2) Kragh-Hansen, U.; Chuang, V. T. G.; Otagiri, M. Practical Aspects of the Ligand-Binding and Enzymatic Properties of Human Serum Albumin. *Biol. Pharm. Bull.* **2002**, *25*, 695−704.

(3) Fanali, G.; di Masi, A.; Trezza, V.; Marino, M.; Fasano, M.; Ascenzi, P. Human Serum Albumin: From Bench to Bedside. *Mol. Aspects Med.* **2012**, *33*, 209−290.

(4) Kragh-Hansen, U. Molecular Aspects of Ligand Binding to Serum Albumin. *Pharmacol. Rev.* **1981**, *33*, 17−53.

(5) Belatik, A.; Hotchandani, S.; Carpentier, R.; Tajmir-Riahi, H.-A. Locating the Binding Sites of Pb(II) Ion with Human and Bovine Serum Albumins. *PLoS One* **2012**, *7*, e36723.

(6) Curry, S. Lessons from the Crystallographic Analysis of Small Molecule Binding to Human Serum Albumin. *Drug Metab. Pharmacokinet.* **2009**, *24*, 342−357.

(7) Froehlich, E.; Mandeville, J. S.; Jennings, C. J.; Sedaghat-Herati, R.; Tajmir-Riahi, H. A. Dendrimers Bind Human Serum Albumin. *J. Phys. Chem. B* **2009**, *113*, 6986−6993.

(8) Zhang, M.-F.; Xu, Z.-Q.; Ge, Y.-S.; Jiang, F.-L.; Liu, Y. Binding of Fullerol to Human Serum Albumin: Spectroscopic and Electrochemical Approach. *J. Photochem. Photobiol. B: Biology* **2012**, *108*, 34−43.

(9) Fasano, M.; Curry, S.; Terreno, E.; Galliano, M.; Fanali, G.; Narciso, P.; Notari, S.; Ascenzi, P. The Extraordinary Ligand Binding Properties of Human Serum Albumin. *IUBMB Life* **2005**, *57*, 787−796.

(10) Varshney, A.; Sen, P.; Ahmad, E.; Rehan, M.; Subbarao, N.; Khan, R. H. Ligand Binding Strategies of Human Serum Albumin: How Can the Cargo be Utilized? *Chirality* **2010**, *22*, 77−87.

(11) Yang, F.; Bian, C.; Zhu, L.; Zhao, G.; Huang, Z.; Huang, M. Effect of Human Serum Albumin on Drug Metabolism: Structural Evidence of Esterase Activity of Human Serum Albumin. *J. Struct. Biol.* **2007**, *157*, 348−355.

(12) Zhu, L.; Yang, F.; Chen, L.; Meehan, E. J.; Huang, M. A New Drug Binding Subsite on Human Serum Albumin and Drug−Drug Interaction Studied by X-ray Crystallography. *J. Struct. Biol.* **2008**, *162*, 40−49.

(13) Fleer, R.; Yeh, P.; Amellal, N.; Maury, I.; Fournier, A.; Bacchetta, F.; Baduel, P.; Jung, G.; L'Hôte, H.; Becquart, J.; et al. Stable Multicopy Vectors for High-Level Secretion of Recombinant Human Serum Albumin by Kluyveromyces Yeasts. *Biotechnology* **1991**, *9*, 968−975.

(14) Kobayashi, K. Summary of Recombinant Human Serum Albumin Development. *Biologicals* **2006**, *34*, 55−59.

(15) Chuang, V. T. G.; Kragh-Hansen, U.; Otagiri, M. Pharmaceutical Strategies Utilizing Recombinant Human Serum Albumin. *Pharm. Res.* **2002**, *19*, 569−577.

(16) Otagiri, M.; Chuang, V. T. G. Pharmaceutically Important Pre- and Posttranslational Modifications on Human Serum Albumin. *Biol. Pharm. Bull.* **2009**, *32*, 527−534.

(17) Taguchi, K.; Chuang, V. T. G.; Maruyama, T.; Otagiri, M. Pharmaceutical Aspects of the Recombinant Human Serum Albumin Dimer: Structural Characteristics, Biological Properties, and Medical Applications. *J. Pharm. Sci.* **2012**, *101*, 3033−3046.

(18) Kratz, F.; Elsadek, B. Clinical Impact of Serum Proteins on Drug Delivery. *J. Controlled Release* **2012**, *161*, 429−445.

(19) Komatsu, T.; Nakagawa, A.; Zunszain, P. A.; Curry, S.; Tsuchida, E. Genetic Engineering of the Heme Pocket in Human Serum Albumin: Modulation of O_2 Binding of Iron Protoporphyrin IX by Variation of Distal Amino Acids. *J. Am. Chem. Soc.* **2007**, *129*, 11286−11295.

(20) He, X. M.; Carter, D. C. Atomic Structure and Chemistry of Human Serum Albumin. *Nature* **1992**, *358*, 209−215.
(21) Li, H.; Grigoryan, H.; Funk, W. E.; Lu, S. S.; Rose, S.; Williams, E. R.; Rappaport, S. M. Profiling Cys^{34} Adducts of Human Serum Albumin by Fixed-Step Selected Reaction Monitoring. *Mol. Cell. Proteomics* **2011**, *10*, M110.004606.
(22) Wardell, M.; Wang, Z.; Ho, J. X.; Robert, J.; Ruker, F.; Ruble, J.; Carter, D. C. The Atomic Structure of Human Methemalbumin at 1.9 Å. *Biochem. Biophys. Res. Commun.* **2002**, *291*, 813−819.
(23) Zunszain, P. A.; Ghuman, J.; Komatsu, T.; Tsuchida, E.; Curry, S. Crystal Structural Analysis of Human Serum Albumin Complexed with Hemin and Fatty Acid. *BMC Struct. Biol.* **2003**, *3*, 6.
(24) Sudlow, G.; Birkett, D. J.; Wade, D. N. The Characterization of Two Specific Drug Binding Sites on Human Serum Albumin. *Mol. Pharmacol.* **1975**, *11*, 824−832.
(25) Ghuman, J.; Zunszain, P. A.; Petitpas, I.; Bhattacharya, A. A.; Otagiri, M.; Curry, S. Structural Basis of the Drug-Binding Specificity of Human Serum Albumin. *J. Mol. Biol.* **2005**, *353*, 38−52.
(26) Sjöholm, I.; Ekman, B.; Kober, A.; Ljungstedt-Påhlman, I.; Seiving, B.; Sjödin, T. Binding of Drugs to Human Serum Albumin: XI. The Specificity of Three Binding Sites as Studied with Albumin Immobilized in Microparticles. *Mol. Pharmacol.* **1979**, *16*, 767−777.
(27) Kremer, J. M. H.; Wilting, J.; Janssen, L. H. M. Drug Binding to Human Alpha-1-acid Glycoprotein in Health and Disease. *Pharmacol. Rev.* **1988**, *40*, 1−47.
(28) Charbonneau, D.; Beauregard, M.; Tajmir-Riahi, H.-A. Structural Analysis of Human Serum Albumin Complexes with Cationic Lipids. *J. Phys. Chem. B* **2009**, *113*, 1777−1784.
(29) Chakraborty, B.; Roy, A. S.; Dasgupta, S.; Basu, S. Magnetic Field Effect Corroborated with Docking Study to Explore Photo-induced Electron Transfer in Drug−Protein Interaction. *J. Phys. Chem. A* **2010**, *114*, 13313−13325.
(30) Pileni, M.-P.; Grätzel, M. Light-Induced Redox Reactions of Proflavin in Aqueous and Micellar Solution. *J. Phys. Chem.* **1980**, *84*, 2402−2406.
(31) Neumann, M. G.; Tiera, M. J. The Use of Basic Dyes as Photochemical Probes. *Quim. Nova* **1993**, *16*, 280−287.
(32) de Silvestri, S.; Laporta, P. Time-Resolved and Steady-State Fluorescence Studies of Excited-State Proton-Transfer Reactions of Proflavine. *Chem. Phys. Lett.* **1984**, *103*, 275−280.
(33) Artali, R.; Bombieri, G.; Calabi, L.; Pra, A. D. A Molecular Dynamics Study of Human Serum Albumin Binding Sites. *Il Farmaco* **2005**, *60*, 485−495.
(34) Fujiwara, S.; Amisaki, T. Molecular Dynamics Study of Conformational Changes in Human Serum Albumin by Binding of Fatty Acids. *Proteins: Struct. Funct. Bioinf.* **2006**, *64*, 730−739.
(35) Deeb, O.; Rosales-Hernández, M. C.; Gómez-Castro, C.; Garduño-Juárez, R.; Correa-Basurto, J. Exploration of Human Serum Albumin Binding Sites by Docking and Molecular Dynamics Flexible Ligand−Protein Interactions. *Biopolymers* **2009**, *93*, 161−170.
(36) Jana, S.; Dalapati, S.; Ghosh, S.; Guchhait, N. Potential Charge Transfer Probe Induced Conformational Changes of Model Plasma Protein Human Serum Albumin: Spectroscopic, Molecular Docking, and Molecular Dynamics Simulation Study. *Biopolymers* **2012**, *97*, 766−777.
(37) Olsen, J. M.; Aidas, K.; Kongsted, J. Excited States in Solution through Polarizable Embedding. *J. Chem. Theory Comput.* **2010**, *6*, 3721−3734.
(38) Olsen, J. M. H.; Kongsted, J. Molecular Properties through Polarizable Embedding. *Adv. Quantum Chem.* **2011**, *61*, 107−143.
(39) Zhang, D. W.; Zhang, J. Z. H. Molecular Fractionation with Conjugate Caps for Full Quantum Mechanical Calculation of Protein−Molecule Interaction Energy. *J. Chem. Phys.* **2003**, *119*, 3599−3605.
(40) Rocha-Rinza, T.; Sneskov, K.; Christiansen, O.; Ryde, U.; Kongsted, J. Unraveling the Similarity of the Photoabsorption of Deprotonated p-Coumaric Acid in the Gas Phase and within the Photoactive Yellow Protein. *Phys. Chem. Chem. Phys.* **2011**, *13*, 1585−1589.
(41) Steindal, A. H.; Olsen, J. M. H.; Ruud, K.; Frediani, L.; Kongsted, J. A Combined Quantum Mechanics/Molecular Mechanics Study of the One- and Two-Photon Absorption in the Green Fluorescent Protein. *Phys. Chem. Chem. Phys.* **2012**, *14*, 5440−5451.
(42) List, N. H.; Olsen, J. M. H.; Jensen, H. J. A.; Steindal, A. H.; Kongsted, J. Molecular-Level Insight into the Spectral Tuning Mechanism of the DsRed Chromophore. *J. Phys. Chem. Lett.* **2012**, *3*, 3513−3521.
(43) Murugan, N. A.; Kongsted, J.; Rinkevicius, Z.; Ågren, H. Color Modeling of Protein Optical Probes. *Phys. Chem. Chem. Phys.* **2012**, *14*, 1107−1112.
(44) Case, D. A.; Darden, T. A.; Cheatham, III, T. E.; Simmerling, C. L.; Wang, J.; Duke, R. E.; Luo, R.; Walker, R. C.; Zhang, W.; Merz, K. M.; et al. *Amber 11*; University of California: San Francisco, 2010.
(45) Hehre, W. J.; Ditchfield, R. J.; Pople, J. A. Self−Consistent Molecular Orbital Methods. XII. Further Extensions of Gaussian−Type Basis Sets for Use in Molecular Orbital Studies of Organic Molecules. *J. Chem. Phys.* **1972**, *56*, 2257−2261.
(46) Hariharan, P. C.; Pople, J. A. The Influence of Polarization Functions on Molecular Orbital Hydrogenation Energies. *Theor. Chim. Acta* **1973**, *28*, 213−222.
(47) Frisch, M. J.; Trucks, G. W.; Schlegel, H. B.; Scuseria, G. E.; Robb, M. A.; Cheeseman, J. R.; Scalmani, G.; Barone, V.; Mennucci, B.; Petersson, G. A.; et al. *Gaussian 09, Revision C.01*; Gaussian, Inc.: Wallingford, CT, 2010.
(48) Cornell, W. D.; Cieplak, P.; Bayly, C. I.; Gould, I. R.; Merz, K. M.; Ferguson, D. M.; Spellmeyer, D. C.; Fox, T.; Caldwell, J. W.; Kollman, P. A. A Second Generation Force Field for the Simulation of Proteins, Nucleic Acids, and Organic Molecules. *J. Am. Chem. Soc.* **1995**, *117*, 5179−5197.
(49) Wang, J.; Wolf, R. M.; Caldwell, J. W.; Kollman, P. A.; Case, D. A. Development and Testing of a General Amber Force Field. *J. Comput. Chem.* **2004**, *25*, 1157−1174.
(50) Bayly, C. I.; Cieplak, P.; Cornell, W.; Kollman, P. A. A Well-Behaved Electrostatic Potential Based Method Using Charge Restraints for Deriving Atomic Charges: the RESP Model. *J. Phys. Chem.* **1993**, *97*, 10269−10280.
(51) Wang, J.; Wang, W.; Kollman, P. A.; Case, D. A. Automatic Atom Type and Bond Type Perception in Molecular Mechanical Calculations. *J. Mol. Graphics Modell.* **2006**, *25*, 247−260.
(52) Becke, A. D. Density-Functional Thermochemistry. III. The Role of Exact Exchange. *J. Chem. Phys.* **1993**, *98*, 5648−5652.
(53) Kendall, R. A.; Dunning, T. H.; Harrison, R. J. Electron Affinities of the First-Row Atoms Revisited. Systematic Basis Sets and Wave Functions. *J. Chem. Phys.* **1992**, *96*, 6796−6806.
(54) Dunning, T. H. Gaussian Basis Sets for Use in Correlated Molecular Calculations. I. The Atoms Boron through Neon and Hydrogen. *J. Chem. Phys.* **1989**, *90*, 1007−1023.
(55) Mennucci, B., Cammi, R., Eds. *Continuum solvation models in chemical physics, from theory to applications*; Wiley: Chichester, UK, 2007.
(56) Tomasi, J.; Mennucci, B.; Cammi, R. Quantum Mechanical Continuum Solvation Models. *Chem. Rev.* **2005**, *105*, 2999−3093.
(57) Jorgensen, W. L. Quantum and Statistical Mechanical Studies of Liquids. 10. Transferable Intermolecular Potential Functions for Water, Alcohols, and Ethers. Application to Liquid Water. *J. Am. Chem. Soc.* **1981**, *103*, 335−340.
(58) Olsson, M. H. M.; Søndergaard, C. R.; Rostkowski, M.; Jensen, J. H. PROPKA3: Consistent Treatment of Internal and Surface Residues in Empirical pK_a Predictions. *J. Chem. Theory Comput.* **2011**, *7*, 525−537.
(59) Díaz, N.; Suárez, D.; Sordo, T. L.; Merz, K. M., Jr. Molecular Dynamics Study of the IIA Binding Site in Human Serum Albumin: Influence of the Protonation State of Lys195 and Lys199. *J. Med. Chem.* **2001**, *44*, 250−260.
(60) Hornak, V.; Abel, R.; Okur, A.; Strockbine, B.; Roitberg, A.; Simmerling, C. Comparison of Multiple Amber Force Fields and Development of Improved Protein Backbone Parameters. *Proteins: Struct. Funct. Bioinf.* **2006**, *65*, 712−725.

(61) Miyamoto, S.; Kollman, P. A. Settle: An Analytical Version of the SHAKE and RATTLE Algorithm for Rigid Water Models. *J. Comput. Chem.* **1992**, *13*, 952−962.
(62) Ryckaert, J.-P.; Ciccotti, G.; Berendsen, H. J. C. Numerical Integration of the Cartesian Equations of Motion of a System with Constraints: Molecular Dynamics of n-Alkanes. *J. Comput. Phys.* **1977**, *23*, 327−341.
(63) Petersilka, M.; Grossmann, U. J.; Gross, E. K. U. Excitation Energies from Time-Dependent Density-Functional Theory. *Phys. Rev. Lett.* **1996**, *76*, 1212−1215.
(64) Salek, P.; Vahtras, O.; Helgaker, T.; Ågren, H. Density-Functional Theory of Linear and Nonlinear Time-Dependent Molecular Properties. *J. Chem. Phys.* **2002**, *117*, 9630−9645.
(65) Dalton, a Molecular Electronic Structure Program, Release Dalton2011, 2011. http://daltonprogram.org/.
(66) Yanai, T.; Tew, D. P.; Handy, N. C. A New Hybrid Exchange−Correlation Functional using the Coulomb-Attenuating Method (CAM-B3LYP). *Chem. Phys. Lett.* **2004**, *393*, 51−57.
(67) Peach, M. J. G.; Helgaker, T.; Sałek, P.; Keal, T. W.; Lutnæs, O. B.; Tozer, D. J.; Handy, N. C. Assessment of a Coulomb-Attenuated Exchange−Correlation Energy Functional. *Phys. Chem. Chem. Phys.* **2006**, *8*, 558−562.
(68) Peach, M. J. G.; Benfield, P.; Helgaker, T.; Tozer, D. J. Excitation Energies in Density Functional Theory: An Evaluation and a Diagnostic Test. *J. Chem. Phys.* **2008**, *128*, 044118.
(69) Aidas, K.; Møgelhøj, A.; Nilsson, E. J. K.; Johnson, M. S.; Mikkelsen, K. V.; Christiansen, O.; Söderhjelm, P.; Kongsted, J. On the Performance of Quantum Chemical Methods to Predict Solvatochromic Effects: The Case of Acrolein in Aqueous Solution. *J. Chem. Phys.* **2008**, *128*, 194503.
(70) Gagliardi, L.; Lindh, R.; Karlström, G. Local Properties of Quantum Chemical Systems: The LoProp Approach. *J. Chem. Phys.* **2004**, *121*, 4494−4500.
(71) Aquilante, F.; De Vico, L.; Ferré, N.; Ghigo, G.; Malmqvist, P.-A.; Neogrády, P.; Pedersen, T. B.; Pitoňák, M.; Reiher, M.; Roos, B. O.; et al. MOLCAS 7: The Next Generation. *J. Comput. Chem.* **2010**, *31*, 224−247.
(72) Söderhjelm, P.; Ryde, U. How Accurate Can a Force Field Become? A Polarizable Multipole Model Combined with Fragment-wise Quantum-Mechanical Calculations. *J. Phys. Chem. A* **2009**, *113*, 617−627.
(73) Ahlström, P.; Wallqvist, A.; Engström, S.; Jönsson, B. A Molecular Dynamics Study of Polarizable Water. *Mol. Phys.* **1989**, *68*, 563−581.
(74) Trott, O.; Olson, A. J. AutoDock Vina: Improving the Speed and Accuracy of Docking with a New Scoring Function, Efficient Optimization, and Multithreading. *J. Comput. Chem.* **2010**, *31*, 455−461.
(75) Sanner, M. F. Python: A Programming Language for Software Integration and Development. *J. Mol. Graphics Modell.* **1999**, *17*, 57−61.
(76) Kongsted, J.; Osted, A.; Pedersen, T. B.; Mikkelsen, K. V.; Christiansen, O. The n→π^* Electronic Transition in Microsolvated Formaldehyde. A Coupled Cluster and Combined Coupled Cluster/Molecular Mechanics Study. *J. Phys. Chem. A* **2004**, *108*, 8624−8632.
(77) Christiansen, O.; Hättig, C.; Gauss, J. Polarizabilities of CO, N_2, HF, Ne, BH, and CH^+ from *ab initio* Calculations: Systematic Studies of Electron Correlation, Basis Set Errors, and Vibrational Contributions. *J. Chem. Phys.* **1998**, *109*, 4745−4757.
(78) Jensen, F. Polarization Consistent Basis Sets. III. The Importance of Diffuse Functions. *J. Chem. Phys.* **2002**, *117*, 9234−9240.
(79) Klimeš, J.; Michaelides, A. Perspective: Advances and Challenges in Treating van der Waals Dispersion Forces in Density Functional Theory. *J. Chem. Phys.* **2012**, *137*, 120901.
(80) van Mourik, T.; Gdanitz, R. J. A Critical Note on Density Functional Theory Studies on Rare-Gas Dimers. *J. Chem. Phys.* **2002**, *116*, 9620−9623.
(81) Jacquemin, D.; Wathelet, V.; Perpète, E. A.; Adamo, C. Extensive TD-DFT Benchmark: Singlet-Excited States of Organic Molecules. *J. Chem. Theory Comput.* **2009**, *5*, 2420−2435.
(82) Uppsten, M.; Durbeej, B. Quantum Chemical Comparison of Vertical, Adiabatic, and 0−0 Excitation Energies: The PYP and GFP Chromophores. *J. Comput. Chem.* **2012**, *33*, 1892−1901.
(83) Whitmore, L.; Wallace, B. A. Protein Secondary Structure Analyses from Circular Dichroism Spectroscopy: Methods and Reference Databases. *Biopolymers* **2008**, *89*, 392−400.
(84) Stone, A. J. Intermolecular Potentials. *Science* **2008**, *321*, 787−789.
(85) Söderhjelm, P.; Kongsted, J.; Ryde, U. Conformational Dependence of Isotropic Polarizabilities. *J. Chem. Theory Comput.* **2011**, *7*, 1404−1414.
(86) Söderhjelm, P.; Krogh, J. W.; Karlström, G.; Ryde, U.; Lindh, R. Accuracy of Distributed Multipoles and Polarizabilities: Comparison between the LoProp and MpProp Models. *J. Comput. Chem.* **2007**, *28*, 1083−1090.
(87) Bagno, A.; Rastrelli, F.; Saielli, G. Prediction of the ^1H and ^{13}C NMR Spectra of α-D-Glucose in Water by DFT Methods and MD Simulations. *J. Org. Chem.* **2007**, *72*, 7373−7381.
(88) Eriksen, J. J.; Olsen, J. M. H.; Aidas, K.; Ågren, H.; Mikkelsen, K. V.; Kongsted, J. Computational Protocols for Prediction of Solute NMR Relative Chemical Shifts. A Case Study of L-Tryptophan in Aqueous Solution. *J. Comput. Chem.* **2011**, *32*, 2853−2864.
(89) Murugan, N. A.; Ågren, H. Role of Dynamic Flexibility in Computing Solvatochromic Properties of Dye−Solvent Systems: o-Betaine in Water. *J. Phys. Chem. A* **2009**, *113*, 2572−2577.